Failure Assessments for MQXF Magnet Support Structure With a Graded Approach

Heng Pan, Eric C. Anderssen, Daniel W. Cheng, Soren O. Prestemon, and Giorgio Ambrosio

***Abstract*—The high luminosity large hadron collider (LHC) upgrade requires new quadrupoles, MQXF, to replace the present LHC inner triplet magnets. The MQXFA magnet is the first prototype that has a 150-mm aperture and uses Nb_3Sn superconducting technology in a 4.2-m magnetic length structure. The support structure design of the MQXFA magnet is based on the bladder-and-key technology, where a relatively low pre-stress at room temperature is increased to the final preload targets during the cool-down by the differential thermal contraction of the various components. The magnet support structure components experience different load levels from pre-load to cool-down and excitation. Consequently, a few parts experience high stresses that may cause localized plastic deformations or internal fracture development. The concept presented in this paper for the failure assessment of support structures integrates nonlinear finite-element (FE) analysis with detailed submodels and fracture mechanics into an advanced engineering tool. The nonlinear FE solutions enable estimations of the structural response to the given loads, and the advanced fracture analysis with failure assessment diagram assesses the structure safety index of results obtained from the FE model. The paper describes how the MQXFA end-shell segments are being optimized based on the failure analyses.**

***Index Terms*—Fracture analysis, Nb_3Sn magnet, mechanical analysis, superconducting magnet.**

I. Introduction

THE Large Hadron Collider High Luminosity upgrade (HL-LHC) project requires new low-β quadrupole magnets, called MQXF, in the Interaction Region (IR) to increase the LHC peak and integrated luminosity [1]. The MQXF magnets designed and fabricated in collaboration between CERN and the U.S. LARP, will serve as Q1, Q2, and Q3 focusing elements in the interaction regions of the HL-LHC. The Q1 and Q3 magnet, referred to as MQXFA, use the Nb_3Sn superconductor technology with 150 mm aperture and a 4.2 m magnetic length and is the first long prototype of the final MQXF design [2].

Manuscript received October 29, 2018; accepted March 25, 2019. Date of publication March 29, 2019; date of current version April 18, 2019. This work was supported in part by the U.S. Department of Energy, Office of Science, Office of High Energy Physics, through the U.S. LHC Accelerator Research Program (until 2018) and through the U.S. HL-LHC Accelerator Upgrade Project (from 2018), and in part by the High Luminosity LHC project at CERN. *(Corresponding author: Heng Pan.)*

H. Pan, E. C. Anderssen, D. W. Cheng, and S. O. Prestemon are with Lawrence Berkeley Laboratory, Berkeley, CA 94720 USA (e-mail: hengpan@lbl.gov).

G. Ambrosio is with Fermi National Accelerator Laboratory, Batavia, IL 80510 USA.

Color versions of one or more of the figures in this paper are available online at http://ieeexplore.ieee.org.

Digital Object Identifier 10.1109/TASC.2019.2908113

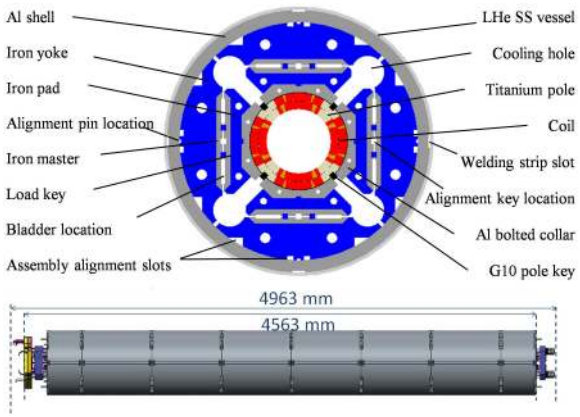

Fig. 1. Cross-sectional and longitudinal view of MQXFA magnet (Al: Aluminum; LHe: Liquid Helium; SS: Stainless Steel.).

The design for MQXF magnets uses a shell-based support structure with the bladder-and-key concept to counteract nominal forces of $+2.47/-3.48$ MN/m (F_x/F_y) without overstressing the brittle Nb_3Sn coils (azimuthal stress in the coil up to 120 MPa at room temperature and 200 MPa at cold can be tolerated without permanent degradation of the conductor properties in the transverse plane [3]). The MQXF magnet aluminum shells, (as shown in Fig. 1) are loaded in tension to preload the magnet coils at room temperature, and then the final pre-load is achieved by thermal contraction during the cool-down phase. The tie rods (not shown in Fig. 1) are also tensioned to load the superconducting coils axially [4].

The mechanical structure of the MQXF magnet is subject to different load levels from pre-load to cool-down and powering. As a result, the aluminum shells and iron yokes experience high stresses at various points during the primary load cases as defined below [5]:

1) Assembly load (1a) and static preload (1b) at room temperature. Load (1a) represents the condition when pressurizing the bladders, and load (1b) is the static load with only the load (interference) keys.
2) Cool-down to 1.9 K. The resulting load condition includes the room-temperature loads and thermal stresses induced by the differential thermal contraction of the structure components.
3) Operation. The magnet is subjected to Lorentz forces in normal operations. The total loads include loads (1b) and (2), the loads induced by cooldown, and the Lorentz forces during energization to full current.

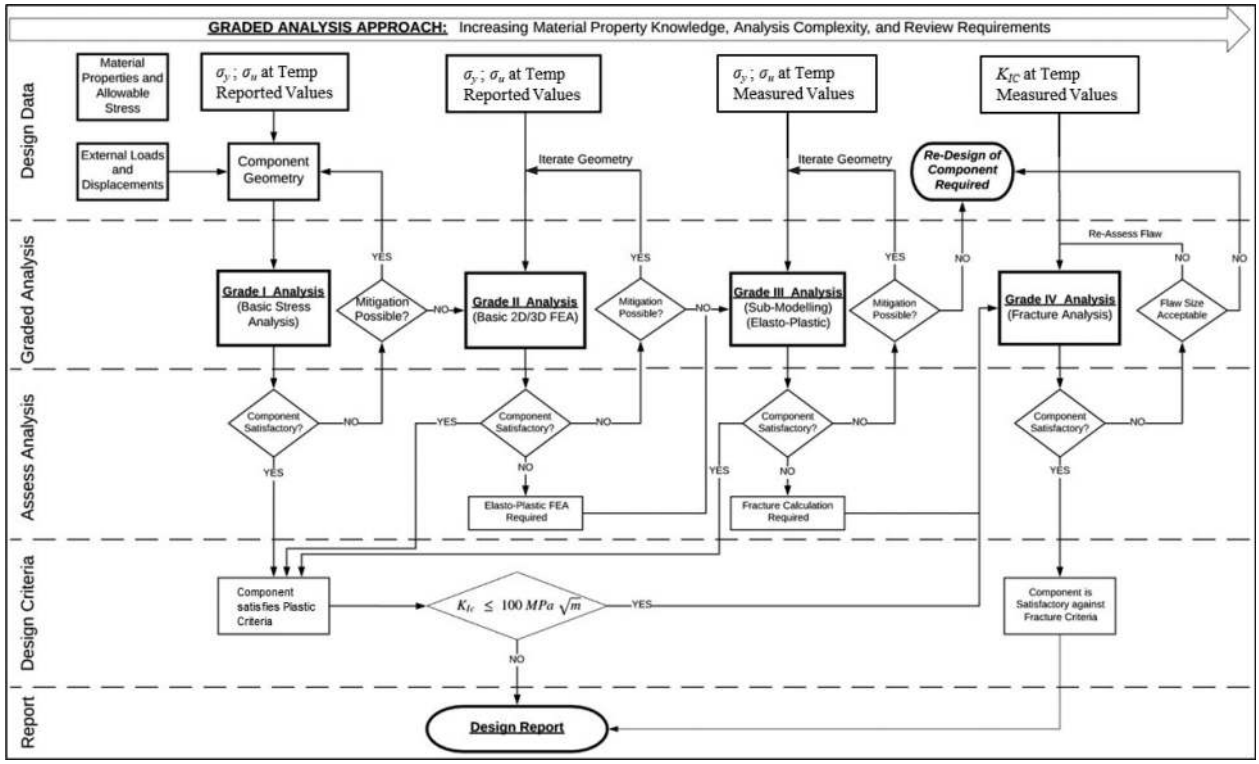

Fig. 2. Schematic of graded approach to analysis procedures.

4) Fault loads represent the loads outside of standard fabrication process and operation.

In order to analyze the potential mechanical failures, such as plastic deformation and fracture development, a graded approach is used for the MQXF magnet. Different criteria are defined in this approach. If criteria defined at each grade are exceeded, it will trigger the next level of analysis and/or require modifications to the design.

In this paper, we describe the case studies for the end-shell and yoke of the MQXFA magnet by implementing the graded approach with FEA models.

II. Graded Mechanical Analysis Procures

For MQXF magnets, structural failures can occur via one of the following:

1) Plastic collapse typically associated with materials that yield in a smooth manner under the influence of large loads;
2) Linear elastic fracture, typically associated with brittle materials under significant loads coupled with stress concentration factors such as defects or voids;
3) Ductile tearing, i.e., materials are subjected to a combination of the elements above.

Failure assessments for MQXFA structure account for the failures above by referencing ASME FFS-1 (Fitness-for-Service) [6] as a standard to accept use of nominally "brittle" materials with assumed flaws. The graded approach, proposed in [5] and shown in Fig. 2, is expected to yield structural designs that are safe for operation in the HL-LHC, and is used in MQXFA designs. The key elements of the terminology used in this graded analysis are taken from established design criteria documents for magnet systems [7], [8].

The graded approach consists of four levels of analysis, in the order of growing model fidelity: (I) simple, analytical formulation (II) Finite Element Analysis (FEA); (III) advanced FEA; (IV) Linear Elastic Fracture Mechanics (LEFM) analysis. Each grade, if not satisfied, has two possible options: (a) re-design the part, or (b) perform a more detailed analysis.

In most cases elastic FEA (Grade II) is enough, and one can redesign the part if the criteria are not met. However, an elasto-plastic FEA (Grade III) is required if the elastic solution is not solvable at areas of stress concentration as in certain complicated parts. Similarly, if the design is still not satisfactory the part can be redesigned, or a fracture analysis (Grade IV) can be performed. Finally, if the part fails the Grade IV analysis the part must be redesigned. Once a part has been redesigned the graded approach restarts from Grade II to verify the new design.

In parallel with Grades II and III analyses, a Grade IV analysis will also be required if brittle materials are involved in the structure. Materials with fracture toughness (K_{IC}) less than 100 MPa $\cdot \sqrt{\text{m}}$ are considered as brittle in this study.

MQXFA structural design uses FEA for every structural component. For most Grade I and II analyses, the FEA results are considered satisfactory when the results meet Von Mises criteria. However, a Grade III analysis is required when the results show either stress singularities (concentrations) or any other resultant loads that exceed the Von Mises criteria. FEA sub-models are also used in this grade to determine the stress concentration factor. Grade IV analyses is required due to the presence of brittle materials where fracture failure mode dominates. This approach relies on the R6 design criteria approach [9], which has been

TABLE I
PEAK STRESSES IN THE METALLIC PARTS OF MQXFAP2 MAGNET (MPA)

Part	Material	Principal Stress		Von Mises Stress		$\sigma_{0.2}$	
		293 K	1.9 K	293 K	1.9 K	293 K	1.9 K
Collar	Al 6061	-	-	121	273	420	550
SS Pad	SS 316	-	-	82	277	289	375
Iron Pad	ARMCO® Pure Iron	98	152	-	-	223 [10]	-
Yoke	ARMCO® Pure Iron	246	306	-	-	223	-
Shell	Al 7075	-	-	320	573	420	550
Endplate	Nitronic 50	-	-	137	333	517	-

adopted by ASME FFS-1 standard. The Failure Assessment Diagram (FAD) is the key tool used in Grade IV analyses since it includes the full range of failure modes listed above.

Due to the complexity of the magnet design and the various load conditions encountered during fabrication, assembly, and operation, the results of 3D FEA models are used for the failure assessments of the MQXFA structural elements. Stress concentrations, observed from the Grade II analysis, are present in the end-shell and yoke, and both parts' materials are considered as low K_{IC} components. Therefore, we use the end-shell and yokes as examples to illustrate the analyses in light of the defined graded approach.

III. CASE STUDY OF THE GRADED II - GENERAL FINITE ELEMENT ANALYSIS

The MQXFA magnet was analyzed at a Grade II level with the general 3D ANSYS model described in [4]. The model applies the azimuthal interference of 750 μm, as defined for MQXFAP2 prototype magnet and the axial preload is provided by pre-tensioning 580 $\mu\varepsilon$ on the stainless steel axial rods.

The simulations include the (1b), (2), and (3) load conditions: the static preload, the cool-down, and loads experienced in normal operations. The peak stresses in the primary structural components are summarized in Table I. Please note Von Mises stresses are used for aluminum collar and stainless steel pads, but principal stresses are used for iron pads and yokes due to their brittle nature.

Additionally, ARMCO Pure Iron (used for the iron pads and yoke) is an ultra high-purity iron produced by AK Steel, was characterized at CERN at both room temperature and 4 K. Brittle fracture was observed in all specimens at cryogenic temperature, thus no yield strength ($\sigma_{0.2}$) was determined from the test campaign [10].

As seen in Table I, most of the structural components are within the yield limits ($\sigma_{0.2}$); therefore, these parts have successfully passed the Grade II analysis and further analysis is not necessary.

The shells and yokes, however, clearly exceed their yield limits at either room temperature or 1.9 K, which is not satisfactory for the Grade II criteria. The peak stresses in the end-shell and yokes are located at the cut-out inner corners, as shown in Fig. 3, which are considered stress concentrations due to the sharp corners in the model. While the shell is loaded in tension the yokes are loaded in compression by the shell. The shell cutouts of the end-shell experience bending at the corners, which is an

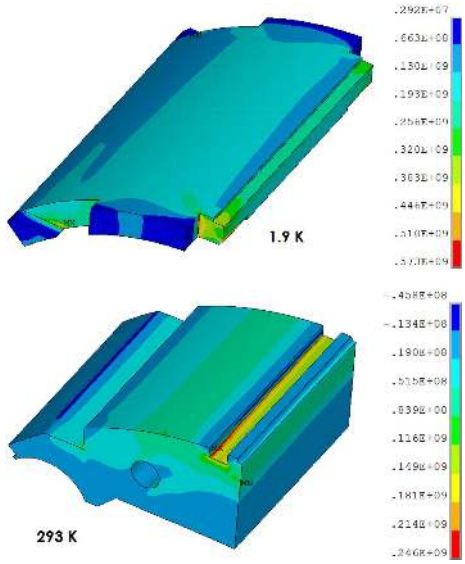

Fig. 3. Von Mises stress distribution (Pa) in the end-shell (top) and principal stress distribution (Pa) in yoke (bottom).

"end effect". The yoke laminations, on the other hand, experience bending in the azimuthal direction that yields a tensile load around the top cut-out corner.

To confirm the peak stress, grid refinement is required. Because of the geometric discontinuity, a model with sharp corners cannot converge with an increase in mesh density. This usually indicates that geometric features, such as fillets or chamfers, need to be included in the model.

The geometric cutouts on shell and yokes are designed for certain functions; the redesign of these parts becomes relatively difficult in terms of the project schedules. In order to resolve the stress concentration in the end-shell and yoke, Grade III analyses with detailed features and mesh refinements are required, as illustrated in Fig. 2.

IV. CASE STUDY OF GRADE III - ADVANCED FEA

For components exhibiting stress concentrations that cannot be readily resolved via routine mesh refinement studies in the primary ANSYS model, sub-modeling was performed to evaluate the stress distribution around the concerning area.

A sub-model is a separate FEA model of the local region of interest, which imposes displacements on the cutting boundaries from the original model. The sub-model boundary stresses must be compared with the original model stresses to verify that St. Venant's principle is valid for the sub-model. The requirement can be expressed:

$$\frac{\|(\sigma_{ij} - \sigma_B) \cdot \vec{n}\|}{\|\sigma_{ij} \cdot \vec{n}\|} \ll 1 \tag{1}$$

where σ_{ij} is the calculated stress tensor after refinement in the sub-model, i and j represent stress tensor direction, and σ_B is the stress tensor at the same location as σ_{ij} from the original full model.

The end-shell and yoke lamination sub-models are shown in Fig. 4, and the addition of a fillet feature in the shell sub-model can be seen as well.

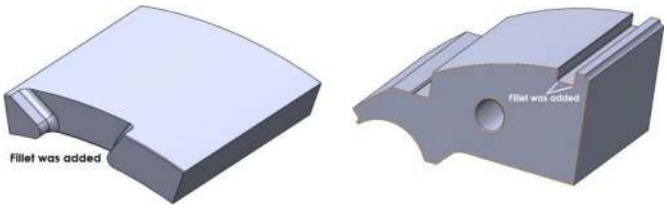

Fig. 4. Sub-models of end-shell and yoke with fillets according to the machining capability.

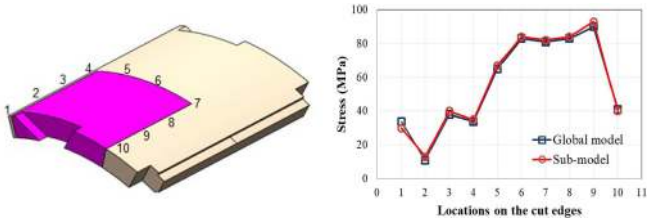

Fig. 5. End-shell sub-model verification using St. Venant's principle, the pink part is the sub-model of the end-shell.

Fig. 5 illuminates the example of the verification for the end-shell sub-model. The Von Mises stress on the selected locations of the sub-model is compared with the stress on the same locations abstracted from the original model. The agreement of the two sets of stress results indicates that the cutting boundaries of the sub-model are remote enough to meet St. Venant's principle, therefore the results of this sub-model are considered valid. The same verification process has been performed on the yoke sub-model.

A. Results of the End-Shell Sub-Model

Thorough grid refinement studies are carried out to verify that the resultant peak stress is reliably determined, and an elastic region is established. The study uses the term of relative mesh density m_i, which is defined as:

$$m_i = \frac{\delta_o}{\delta_i} \tag{2}$$

where δ_o and δ_i are the size of the pyramid element in the original global model and in the sub-model, respectively. δ_o is 8 mm for the end-shell in the original model.

Fig. 6 shows the grid refinement study of the end-shell sub-model. The peak stress in end-shell increases and finally converges when the relative mesh density is over 10. Thus, the subsequent studies use element size of 0.8 mm.

Three fillet radii are taken into account in the mesh refinement studies. The peak stress decreases to 490 MPa with 5 mm fillet at 1.9 K, which is within the yield limits of 550 MPa for Al 7075-T6.

B. Results of the Yoke Sub-Model

The ARMCO Pure Iron used for yokes is considered brittle at 1.9 K according to the test results conducted at CERN [10]. Again, a sub-model was used to determine the plastic deformation and stress on a predicted path if part-through a crack appears. Similarly, the yoke sub-model also compares three different fillet radii in the geometry (Fig. 7). Additionally, as seen on the

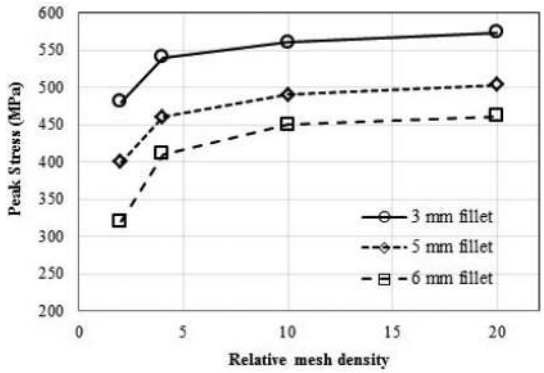

Fig. 6. Relationship between the shell peak Von Mises stresses at the stress concentration area and the relative mesh density m_i, calculated at 1.9 K. Marks of circle, diamond, and square represent fillet radius of 3 mm, 5 mm, and 6 mm at that corner.

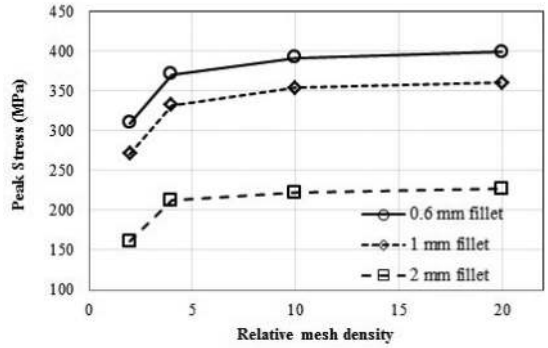

Fig. 7. Relationship between the yoke peak principal stresses at the stress concentration area and the relative mesh density m_i. The stress is calculated at room temperature. Marks of circle, diamond, and square represent fillet radius of 0.6 mm, 1 mm, and 2 mm at that corner.

end-shell sub-model, the yoke peak stress converges with the mesh densities. The subsequent studies used the relative mesh density of 10 as well.

By adding fillets around the high stress areas, stress concentrations in the end-shell and yoke are resolved to a certain degree. However, both Al 7075-T6 and iron do not exhibit significant strain hardening [11], and the K_{IC} is still low at both room temperature and 1.9 K. Therefore, as stated earlier, a Grade IV analysis using LEFM with the sub-model solutions is required to assess the failure of an end-shell with flaws the size determined by the quality assurance process.

V. Case Study of Grade IV - Fracture Failure Assessment

As stated in Section II, the end-shell and yoke lamination are considered as fracture dominant materials due to low K_{IC}. Those parts also exhibit high stresses at some local points. A Grade IV fracture analysis is triggered to determine the potential critical flaw size for non-destructive evaluation for flaws as part of the quality assurance process.

A. Fracture Analysis Method

As the materials exhibit fracture failure modes at both room and cryogenic temperature, fracture failure assessments for the

end-shell and yoke with given flaw sizes were performed at Grade IV, per Fig. 2.

As mentioned in Section II, the fracture failure assessment in this step relies on the R6 FAD, which captures failure by LEFM, and plastic collapse simultaneously.

For the purposes of design, semi-elliptic part-through cracks are assumed with flaw features intersecting, and centered on, the components' surface, as these typically have the highest stress intensities. The major process is to determine the applied stress intensity K_I. For part-through cracks subject to primary stresses, K_I can be written in the following form [12]:

$$K_I = F\sigma(x)\sqrt{\frac{\pi a}{Q}} \tag{3}$$

$$Q = 1 + 1.464\left[\frac{a}{c}\right]^{1.65} \tag{4}$$

where, a and c are the minor and major elliptical radius of a crack. Q is the flaw shape parameter, which is a function of the ratio *a/c*. F is a geometric constant that can be obtained from FEA model or published data. $\sigma(x)$ can be approximated as a cubic expansion of a load profile extracted from an unflawed elastic analysis in the direction of assumed crack propagation through part thickness $x = a$ direction. $F\sigma(x)$ can be approximated as:

$$F\sigma(x) = \sum_{i=0}^{3} G_i A_i x^i \tag{5}$$

where, G_i is an influence coefficient for a part-through internal flaw in a cylinder; A_i is the curve-fitting coefficient of the stress profile along the path of assumed crack propagation. This predicted crack path in the sub-models starts at the point of stress concentration, and points to the direction of the lowest stress gradient, and is normal to the maximum principal stress.

With the total stress abstracted from the sub-model FEA solutions and a given crack length, the load point of each case can be determined in the FAD. Load points inside of the FAD curve are safe from failure; load points falling outside or on the curve may fail. Each load point determines a load line by connecting the origin. The load factor γ_{LF} in the plot is defined as:

$$\gamma_{LF} = \frac{L}{L'} \tag{6}$$

where, L is the length from the original point to the load point; L' is the length from the original point to the projected load point, which is the intersection of load line and the FAD curve. A flaw is considered critical in size if its Load Factor is unity.

B. Fracture Assessment for the End-Shell

Fig. 8 shows the total Von Mises stresses on a predicted crack path in the end-shell with two different fillets at 1.9 K. As defined above, the predicted path of a crack on the end-shell is from the spot of stress concentration to the inner surface of the shell with a depression angle of 20° respect to the outer surface of the shell.

The local stress concentration results in local plastic deformations that limit the effective stress state. The fully elastic analysis will coincide with the elasto-plastic model at some distance from the structural discontinuity. The distance to the coincidence is

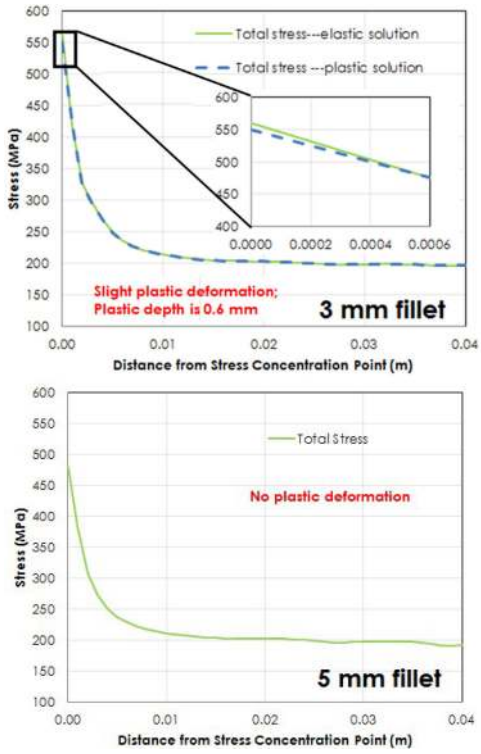

Fig. 8. Total stress on the path of a crack is most likely to propagate in the end-shell.

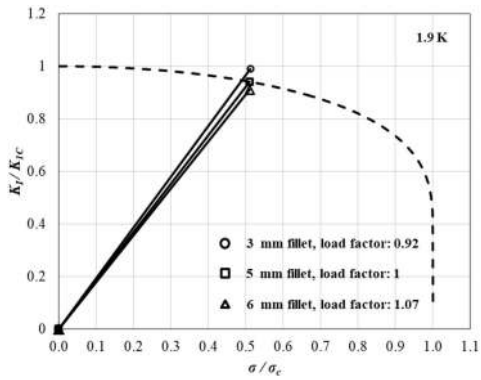

Fig. 9. FAD for 2 mm crack in stress concentration area of end-shell with different fillet sizes, σ_y is the yield stress.

considered as the plastic depth on the defined path. With a 3 mm fillet, plastic deformation occurred around the area of stress concentration, resulting in a 0.6 mm plastic depth along the path. However, the peak stress dropped when increasing the fillet radius to 5 mm.

A flaw that is smaller than the critical size will not propagate. The fracture toughness K_{IC} used in the FAD is 20 MPa $\cdot \sqrt{\text{m}}$ as reported in [13]. The critical flaw size of the case of 5 mm fillet is 2 mm at 1.9 K. Similarly, the critical flaw sizes are 1.6 mm and 2.5 mm for the cases of 3 mm and 6 mm fillet, respectively. As a result, the FAD calculation for the end-shell cutout assumes that a 2 mm crack initiates at the area of stress concentration. Fig. 9 illustrates the calculated load points in the FAD of the stress concentration area with different fillet radii. As expected, the

TABLE II
FLAW SIZES CORRELATED TO INSPECTION GRADES FOR ALUMINUM FORGINGS [14]

Inspection Class	Calibration Block	Allowable Critical Flaw Size
AAA	0.40 mm	> 0.90 mm
AA	0.79 mm	> 1.77 mm
A	1.19 mm	> 2.67 mm
B	1.98 mm	> 4.44 mm

load factor is positively correlated to the fillet size. To maintain a load factor larger than 1, one should ensure the fillet radius is at least 5 mm. As pointed out in Fig. 2, re-designing of the component is suggested, which was done by adding proper fillets in this case.

Components used in MQXFA with material that are considered brittle will require inspection for flaws of critical size. Detection limits for ultrasonic methods in wrought aluminum (and most other standards) are calibrated to circular flaws based on grade, described in ASTM B594 [14]. The calibration flaws for inspection class are shown in Table II. For a flaw of 2 mm, an inspection Class of "AA" is required; a higher Class of "AAA" is required if a flaw smaller than 1.77 mm must be detected. Components which do not pass inspection will either be rejected, or quarantined for further examination.

As a reminder, the K_{IC} used in these assessments is the lowest reported value for plate materials. It is possible that a higher value may be achieved in the actual material batches used, although it is also possible the K_{IC} could be lower. This assessment will be repeated with measured data for the shell forgings.

Note that the load factor of 1 is only at this area of stress concentration; the load factor in the majority of the shell material is larger than 1.4. However, based on the lowest load factor, the cut-out corners of the end-shell were modified with a 5 mm fillet. Additionally, each batch of the forged material will be ultrasonically inspected per Class "AA" criteria for flaws.

C. Fracture Assessment for the Yoke

The yoke yields at the notch corner at room temperature in the cases of fillet radius from 0.6 mm to 2 mm. The top notch experiences a bending moment due to the compression from the shell. As a result, the predicted crack path is from the notch corner (stress concentration) towards the hole (Fig. 4).

Fig. 10 shows the total principal stress on this crack path at room and cryogenic temperature. The depths of the plastic deformation at room temperature are 2.1 mm and 0.8 mm for the cases of fillet radius with 1 mm and 2 mm, respectively. As lack of the measured yield strength at 1.9 K, only the total stresses at 1.9 K of both cases are presented in Fig. 10.

The fracture toughness of the ARMCO Pure Iron is 24.1 MPa $\cdot \sqrt{\text{m}}$ as reported in [15]. According to the total stress illustrated in Fig. 10, the critical flaw sizes for the case of 1 mm fillet are calculated as 8.6 mm and 5.5 mm at room temperature and 1.9 K. The calculated critical flaw size is much larger than the plastic zone seen on yoke.

The FAD of yoke with the assumption of 5 mm flaw size is shown in Fig. 11. The load points of cases of 1 mm and 2 mm fillets are within the safety limit of the FAD. The results

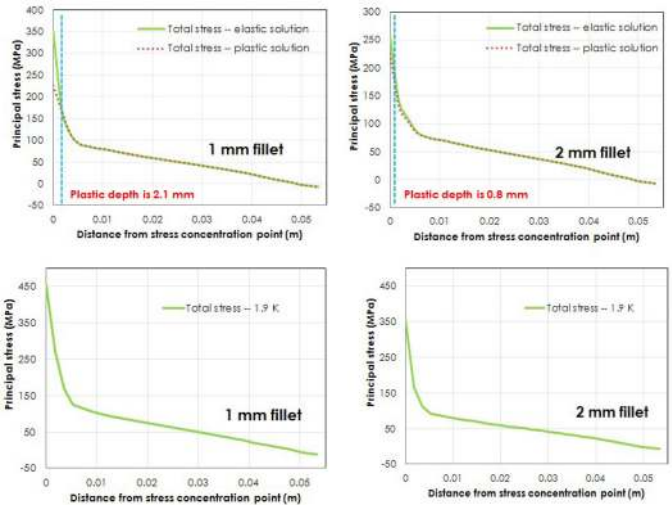

Fig. 10. Total stress on the yoke along the path at room temperature and 1.9 K with fillet radiuses of 1 mm and 2 mm.

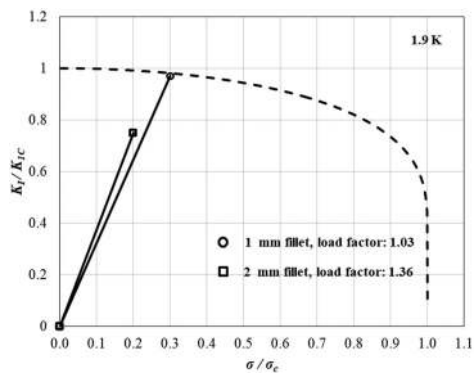

Fig. 11. FAD for 5 mm thumbnail crack in the stress concentration area of the yoke with different fillet sizes, σ_y is the yield stress.

indicate that 2 mm fillet will be adequate for yoke at both room temperature and 1.9 K.

VI. CONCLUSION

Failure assessments for the MQXFA magnet structural metallic parts have been performed in light of a graded approach. Most of the structural components meet the design criteria at Grade II level. However, stress concentrations were found on the end-shell and yoke, which triggered a Grade III advanced mechanical analysis. The end-shell and yoke are also considered brittle materials; therefore a Grade IV fracture assessment was performed as well. The analysis suggests that adding fillets on the cut-out corners of these components will reduce the stress concentration and also release the elastic energy if a local flaw is present; a 5 mm fillet on the shell cut-outs and 2 mm fillets on the yokes were shown to be sufficient.

While the case studies presented here focus on the MQXFA magnet, the general approach presented in this paper can also be used in analyzing the structural components (excluding pressure vessels) of other superconducting magnets in general.

REFERENCES

[1] P. Ferracin *et al.*, "Development of MQXF: The Nb_3Sn low-β quadrupole for the HiLumi LHC," *IEEE Trans. Appl. Supercond.*, vol. 26, no. 4, Jun. 2016, Art. no. 4000207.

[2] H. Pan *et al.*, "Assembly tests of the first Nb_3Sn low-beta quadrupole short model for the Hi-Lumi LHC upgrade," *IEEE Trans. Appl. Supercond.*, vol. 26, no. 4, Jun. 2016, Art. no. 4001705.

[3] G. Sabbi *et al.* "US HL-LHC accelerator upgrade project design criteria for MQXFA superconducting elements," Rep. US-HILUMI-DOC-885, 2018.

[4] H. Pan *et al.*, "Mechanical design studies of the MQXF long model quadrupole for the HiLumi," *IEEE Trans. Appl. Supercond.*, vol. 27, no. 4, Jun. 2017, Art. no. 4004105.

[5] S. Prestemon, E. Anderssen, "US HL-LHC accelerator upgrade project structural design criteria," Rep. US-HILUMI-DOC-909, 2018.

[6] ASME Standards Collection - ASME API 579-1/ASME FFS-1 2016.

[7] ITER Structural Design Criteria for Magnet Components (SDC-MC).

[8] NSTX Structural Design Criteria, Rev. 0, 8/01/03.

[9] British Energy Generation Limited, "Assessment of the integrity of structures containing defects," 699 R6 Revision 4, Amendment 7, Apr. 2009.

[10] M. Crouvizier, "Metallurgy ARMCO and MAGNETIL materials," CERN Eng. Rep. EDMS # 1744165, 2017.

[11] J. M. Bloom, "Prediction of ductile tearing of compact fracture specimens using the R-6 failure assessment diagram," *Int. J. Pressure Vessels Piping*, vol. 8, no. 3, pp. 215–231, 1980, doi: 10.1016/0308-0161(80)90026-5.

[12] T. Anderson, *Fracture mechanics—fundamentals and applications*, 2nd ed. Boca Raton, FL, USA: CRC Press, 1994.

[13] ASM Aerospace Specification Metals, "7000 series aluminum alloy," Accessed: Apr. 12, 2017. [Online]. Available: http://asm.matweb.com/search/SpecificMaterial.asp?bassnum=ma7075t6

[14] ASTM B594, "Standard practice for ultrasonic inspection of aluminum-alloy wrought products," 2013.

[15] I. A. Santillana, "Mechanical properties at cryogenic temperature of materials for the yoke of advanced accelerator magnets for the HiLumi LHC upgrade," CERN Eng. Rep. EDMS # 1802379, 2016.